


## Trigonal symmetry breaking and its electronic effects in the two-dimensional dihalides $MX_2$ and trihalides $MX_3$

Alexandru B. Georgescu <sup>1,\*</sup>, Andrew J. Millis <sup>2,3,†</sup> and James M. Rondinelli <sup>1,‡</sup>

<sup>1</sup>*Department of Materials Science and Engineering, Northwestern University, Evanston, Illinois 60208, USA*

<sup>2</sup>*Center for Computational Quantum Physics, Flatiron Institute, 162 5th Avenue, New York, New York 10010, USA*

<sup>3</sup>*Department of Physics, Columbia University, 538 West 120th Street, New York, New York 10027, USA*



(Received 9 November 2021; revised 7 June 2022; accepted 8 June 2022; published 29 June 2022)

We study the consequences of the approximately trigonal ( $D_{3d}$ ) point symmetry of the transition metal ( $M$ ) site in two-dimensional van der Waals  $MX_2$  dihalides and  $MX_3$  trihalides. The trigonal symmetry leads to a 2-2-1 orbital splitting of the transition metal  $d$  shell, which is best represented by  $d$  orbitals that describe the trigonal rather than  $O_h$  symmetry. The ligand-ligand bond length differences (rather than metal-ligand) take the role of a Jahn-Teller-like mode and in combination with interlayer distances and dimensionality effects tune the crystal field splittings and bandwidths. These effects, in turn, are amplified by electronic correlation effects—leading to crystal field splittings of the order of 0.1–1 eV between the singlet and the lowest orbital doublet—as opposed to the often assumed degenerate  $3t_{2g}$  states. Our calculations explain why most of the materials in this family are insulating, and why these considerations have to be taken into account in realistic models of them. Further, orbital order coupled to various lower symmetry lattice modes may lift the remaining orbital degeneracies, and we explain how these may support unique electronic states using  $ZrI_2$  and  $CuCl_2$  as examples, and offer a brief overview of possible electronic configurations in this class of materials. By building and analyzing Wannier models adapted to the appropriate symmetry we examine how the interplay among trigonal symmetry, electronic correlation effects, and  $p$ - $d$  orbital charge transfer leads to insulating, orbitally polarized magnetic and/or orbital-selective Mott states, and we provide a simple framework and numerical tool for others. Our paper establishes a rigorous framework to understand, control, and tune the electronic states in low-dimensional correlated halides. Our analysis shows that trigonal symmetry and its breaking is a key feature of the two-dimensional halides that needs to be accounted for in search of novel electronic states in materials ranging from  $CrI_3$  to  $\alpha$ - $RuCl_3$ .

DOI: [10.1103/PhysRevB.105.245153](https://doi.org/10.1103/PhysRevB.105.245153)

### I. INTRODUCTION

Transition metal compounds exhibit electronic properties of high scientific and technological interest, including ferroelectricity [1–4], quantum magnetism [5–10], metal-insulator transitions (MITs) [11–21], and high transition-temperature superconductivity [22–26]. Transition metal oxides derived from the  $AMO_3$  perovskite structure have been a focus of particular attention because any  $3d$  or  $4d$  transition metal can occupy the  $M$  site with (typically) partially filled  $d$  shells, while variation of the  $A$  site ion can tune the relative valence of the  $M$  site ion and the electronic bandwidth. The perovskite structure is also highly polymorphic. It allows for many variants of the basic structure that exhibit different crystallographic symmetries, which activate interesting electronic states, and the pseudocubic structure allows for a wide variety of superlattices to be built [18,19,27]. Basic to the electronic physics of perovskites is the cubic ( $O_h$ ) point symmetry of the  $M$  site ion and its reduction to tetragonal symmetry by even parity octahedral distortions.

Recently, two-dimensional (2D) van der Waals transition metal  $MX_2$  dihalides and trihalides  $MX_3$  with  $X$  a halogen ligand have become of interest as they exhibit layer-dependent ferromagnetism as in  $VI_3$  [28–33], possible Kitaev spin liquid behavior in  $RuCl_3$  [34–39], and other magnetic phenomena [40–42]. Additionally, the crystal and electronic structures are highly two dimensional, so the materials can be exfoliated, made in monolayer form, doped by gating and layering with other compounds, and potentially twisted into Moiré materials [43]. Similar to the perovskite transition metal oxides, the  $M$  site is sixfold coordinated by ligands and can host essentially all  $3d$  and  $4d$  transition metals often with partial  $d$  orbital occupancy, which endows them with the aforementioned physical properties. Dihalide and trihalide compounds with the same transition metal will exhibit different nominal valence and octahedral coordination. Table I lists structural and electronic features of several known 2D halides.

Although the sixfold coordination of the metal cations in the dihalides and trihalides would suggest octahedral symmetry  $O_h$ , analogous to the octahedral coordination in many perovskite oxides, we argue here that the halides are more appropriately described as trigonally coordinated. A local orbital basis derived from  $e_g$  and  $t_{2g}$  representations of the  $O_h$  group is not the most useful description [44]. As Table I shows, the metal site symmetry in the bulk halides is either trigonal

\*alexandru.georgescu@northwestern.edu

†ajm2010@columbia.edu

‡jrondinelli@northwestern.edu

TABLE I. Symmetry, atomic structure,  $d$ -electron configuration for the metal, and magnetic order of experimental transition metal dihalides and trihalides. AFM, FM, and HM indicate antiferromagnetic, ferromagnetic, and helimagnetic, respectively. MV indicates multiple values for the specified lengths. Structural data are from Ref. [46] and magnetic data are from Ref. [40].

Structure type	CdI <sub>2</sub>	CdCl <sub>2</sub>	BiI <sub>3</sub>	CrCl <sub>3</sub>	AlCl <sub>3</sub>
$X$ packing	hcp	ccp	hcp	ccp	$\sim$ ccp
Space group	$P\bar{3}m1$	$R\bar{3}m$	$R\bar{3}$	$P3_212$	$C2/m$
Point group	$D_{3d}$	$D_{3d}$	$C_{3i}$	$D_3$	$C_{2h}$
Compound	FeI <sub>2</sub>	NiI <sub>2</sub>	FeCl <sub>3</sub>	CrCl <sub>3</sub>	CrI <sub>3</sub>
$M$ - $d^n$ config.	$d^6$	$d^8$	$d^5$	$d^3$	$d^3$
$M$ site sym.	$D_{3d}$	$D_{3d}$	$C_3$	$C_3$	$C_2$
Magnetism	AFM	HM	HM	AFM	FM
$L_1$	4.050	3.927	3.380	3.483	MV
$L_2$	4.110	4.580	3.216	3.228	MV
$L_3$			3.472	3.229	MV
Compound	TiCl <sub>2</sub>	MnCl <sub>2</sub>	VCl <sub>3</sub>	$\alpha$ -RuCl <sub>3</sub>	$\alpha$ -RuCl <sub>3</sub>
$M$ - $d^n$ config.	$d^2$	$d^5$	$d^2$	$d^5$	$d^5$
$M$ site sym.	$D_{3d}$	$D_{3d}$	$C_3$	$C_3$	$C_2$
Magnetism	AFM	AFM, HM	AFM	AFM	
$L_1$	3.430	3.711	3.471	3.44	MV
$L_2$	3.636	3.505	3.366	3.490	MV
$L_3$			3.366	3.487	MV

( $D_{3d}$ ,  $D_3$ ,  $C_{3i}$ ) or a trigonal subgroup ( $C_{2h}$ ) or even lower [40] and, as previously noted for example in  $MX_2$  compounds [45], a basis that conforms to the symmetry enables a more straightforward treatment of the physics.

In this paper, we show that the commonly assumed orbital basis associated with the  $O_h$  group is not the most appropriate choice; rather, the most appropriate choice is a trigonal basis characterized by an upper  $e_g$  doublet (similar to the common one associated with cubic symmetry), a lower  $e_g$  doublet, and an  $a_{1g}$  singlet. The lower three orbitals can be obtained through a rotation from the  $O_h$   $t_{2g}$  orbitals, and allow us to have a basis which is simple to interpret: The density matrix is diagonal, and thus the electronic states have a well-defined filling, with no off-diagonal occupation terms. Electronic states then, particularly in the presence of magnetism and correlations, when a band gap opens, are either occupied or empty. The crystal field splittings in this basis—by analogy to the Jahn-Teller ones observed under a tetragonal distortion in perovskite oxides, for example—are characterized by ligand-ligand bond length differences (which may, in fact, leave metal-ligand bond lengths unaffected). The ligand-ligand distortions, dimensionality reduction (the octahedral network is two dimensional), and interlayer distances all further tune the crystal field splitting between the lower three orbital states, and their relative bandwidths. These effects also tune the crystal field splitting between the lower three and the upper two orbitals. The crystal field splitting between the lowest doublet and the singlet is of the order of 0.1 eV in the absence of correlations, and is strongly amplified by correlations and magnetic order to the order of 1 eV, higher than the effect of other effects in this class of materials—including spin-orbit

coupling. This effect explains why most halides are insulating, including materials with a  $d^1$ ,  $d^2$ ,  $d^4$ , or  $d^5$  electronic configuration on the transition metal site. We also find that the band gap can be controlled by the relative lengths of the ligand-ligand bonds. While the physics is, of course, the same, regardless of the basis, the  $O_h$  basis does not allow for a simple understanding of this physics without an in-depth analysis of the off-diagonal density matrix, which is less intuitive. We then proceed to show how further orbital and lattice symmetry reduction can lead to new, pseudo-one-dimensional (1D) electronic states in this class of materials, and we enumerate a wide variety of possible electronic states. In order to best illustrate how one can obtain a Wannier function following this representation, we also describe a simple procedure, and provide the associated scripts to perform it in [47].

In addressing these questions, it is often helpful to construct a Wannier basis that includes a representation of the local transition metal  $d$  orbitals, which host the electron interactions associated with correlated electron phenomena. However, standard Wannierization procedures for these materials do not easily produce a basis that transforms properly under trigonal symmetry operations. We present a procedure for constructing an appropriate symmetry-adapted basis, which can easily be adapted to other materials. This allows us to discuss the correlated insulating states that may be obtained in stoichiometric compounds, as well as new electronic states that may appear as a result of further symmetry breaking, such as those present in the semi-1D chains in ZrI<sub>2</sub>, and certain polymorphs of RuCl<sub>3</sub>, CrI<sub>3</sub>, and other halides [40].

Although spin-orbit coupling (SOC) is crucial to key aspects of the low energy physics of some of these materials, we do not include it in our analysis here. The crystal field splittings we find from the trigonal symmetry breaking are of the order of 0.1 eV, which is larger even than the characteristic energy scale of spin-orbit coupling in  $4d$  compounds such as Ru (where it is of the order of 0.04 eV); these effects are always key. Our initial focus is to establish a foundation to understand other relevant degrees of freedom in the halides. Spin-orbit coupling effects can then be added as needed for each material. One consequence of SOC is that it often further reduces the orbital symmetry, as shown in recent work on  $MX_2$  compounds [45]. This approach works well in many transition metal oxides, e.g., Ca<sub>2</sub>RuO<sub>4</sub>, where the physics of the metal-insulator transition can be understood without accounting for SOC; only the detailed low energy magnetic structure of the compound requires SOC.

## II. LOCAL STRUCTURE: ELECTRONIC STATES AND SYMMETRY CONSIDERATIONS

The basic structural unit of 2D halides is a plane of transition metal ions, with each transition metal ion coordinated with six halogen ions [Fig. 1(a)]. Unlike in the layered perovskite-based transition metal compounds, the local axes of the octahedron surrounding a transition metal ion in a halide are rotated with respect to the axes that define the two-dimensional plane. Specifically, choosing coordinates such that the monolayer plane is perpendicular to [001], the octahedral axes ( $M$ - $X$  bond directions) are  $[\pm 1 \pm 1 \pm 1]$  in the ideal halides [cf. Figs. 1(b) and 1(c)]. In the ideal monolayer case,

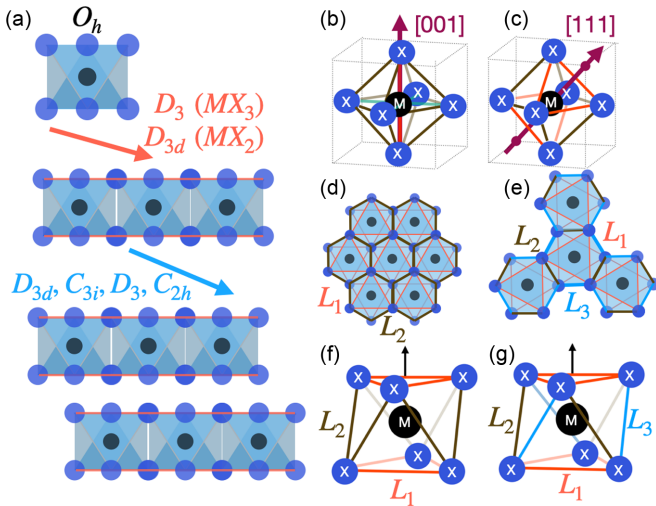


FIG. 1. (a) Sequential illustration of symmetry breaking as a result of the layered structure in dihalides and trihalides. Placing an ideal octahedron within a monolayer will reduce its  $O_h$  symmetry to trigonal  $D_{3d}$  symmetry, for a dihalide octahedron, and  $D_3$  for a trihalide: In both cases, threefold rotations along the  $z$  axis are preserved, as well as inversion symmetry. Three mirror symmetry planes are preserved in the dihalides, but not the trihalides, due to the different octahedral connectivity. Sketch of (b) tetragonal and (c) trigonal symmetry breaking of an octahedron. Heavy magenta arrows indicate the vector normal to monolayer planes. Layer structure of  $MX_6$  octahedra for (d)  $MX_2$  dihalides and (e)  $MX_3$  trihalides. Definitions for halide-halide lengths for octahedra in (f)  $MX_2$  and (g)  $MX_3$  halides. The red edges with length  $L_1$  surround the face parallel to the monolayer planes;  $L_2$  are edges that are not parallel to the material plane and that connect nearest-neighbor  $MX_6$  octahedra.  $L_3$  edges do not connect octahedra, are not parallel to the plane, and only appear in  $MX_3$  compounds.

the point symmetry of the  $M$  ion is then  $D_{3d}$  (for dihalides) or  $D_3$  (for trihalides). The symmetry may be further reduced by spin-orbit coupling, additional relaxations of the atomic positions, magnetic order, and different stackings of the layered structures. We discuss some lattice symmetry reductions as well as magnetic order later.

The key feature of the  $D_3$  and  $D_{3d}$  symmetry is a threefold rotation axis, in the ideal case perpendicular to the monolayer plane of  $MX_6$  octahedra [Figs. 1(d) and 1(e)] and passing through a triangular  $X_3$  face [Figs. 1(f) and 1(g)]. In the full  $D_{3d}$  symmetry found in the dihalides, the  $M$ - $X$  bond lengths remain equal; however, the  $X$ - $X$  ligand distances  $L_i$  ( $i = 1 - 3$ ) need not be equal. The nonequivalence is accommodated through changes in the  $X$ - $M$ - $X$  intraoctahedral angles. Similar effects are known in edge sharing perovskites [48,49]. Because of the planar structure formed by edge connectivity of the octahedra, the halogen-halogen distances perpendicular to (001) [denoted  $L_1$  in Figs. 1(f) and 1(g)] are inequivalent to  $X$ - $X$  distances on other triangular faces. This can be plainly observed in the  $MX_2$  compounds, where  $X$ - $X$  edges not parallel to the plane connect different octahedra, while those that are parallel to the plane connect the same octahedra. This leads to the nonequivalence of the  $L_1$  and  $L_2$   $X$ - $X$  edges [Fig. 1(f)].

One may parametrize the trigonal distortion away from perfect octahedral coordination either by the  $L_2/L_1$  ratio or by the  $X$ - $M$ - $X$  bond angles. We find that the  $L_2/L_1$  ratio is a more convenient parametrization in  $D_{3d}$  symmetry, as it plays an analogous role to the  $c/a$  ratio for the tetragonal symmetry and tunes the splitting between the doublet and singlet. For the  $MX_3$  compounds only half of the  $X$ - $X$  edges not parallel to the plane connect  $MX_6$  octahedra, leading to a total of three inequivalent edges,  $L_1$ ,  $L_2$ , and  $L_3$ . Figure 1(d) illustrates that in both cases there are only two types of inequivalent faces: Those parallel to the planes of  $MX_6$ , with three  $L_1$  edges, and those oblique to the plane with edges  $L_1$ ,  $L_2$ , and  $L_3$ , leading to the lower symmetry group  $D_3$ .

While the symmetry of an ideal dihalide monolayer is  $D_{3d}$  (or  $D_3$  for a trihalide monolayer) different arrangements of the planes can lead to symmetry reductions to  $D_3$  or  $C_{3i}$  in the bulk compounds (see Table I). Both  $D_{3d}$  and  $D_3$ , and these subgroups, however, lead to the same trigonal orbital basis for the transition metal  $M$   $d$  orbitals, imposed by the threefold rotation symmetry axis. Anisotropic semicovalent and van der Waals interactions or additional electronically driven orderings can lead to further symmetry reductions (see Table I). In such cases the clearest way to understand the resulting orbital structure is as an additional symmetry reduction beyond trigonal, leading to a breaking of the doublet degeneracy.

The trigonal symmetry has implications for the electronic structure. Under  $D_{3d}$  symmetry, the five  $d$  orbitals transform as two doublets ( $e_g^\sigma$  and  $e_g^\pi$ ) and a singlet ( $a_{1g}$ ). Under  $D_3$  symmetry the same arguments hold and the same resulting orbitals appear; however, they are more appropriately named  $e$  doublets and an  $a_1$  singlet. For simplicity, and as the orbitals are the same and have the same crystal field splitting relationships, we will generally refer to them as  $e_g$  and  $a_{1g}$ . This is similar to oxides research, where usually the terms  $e_g$  and  $t_{2g}$  are used for orbitals in octahedra-containing compounds even when the crystal symmetry is lower. The wave functions and level splittings are not constrained by symmetry and depend on details of atomic-scale physics. The trigonal structure of the halides may be viewed as a weak distortion of the  $O_h$  symmetry familiar from cubic perovskites, enabling a simpler interpretation of the basis functions. Under  $O_h$  symmetry, the atomic  $d$  orbitals transform as an  $e_g$  symmetry doublet (wave functions conventionally chosen as  $d_{\bar{x}^2-\bar{y}^2}$  and  $d_{3\bar{z}^2-\bar{r}^2}$ ) and a  $t_{2g}$  triplet (wave functions conventionally chosen as  $d_{\bar{x}\bar{y}}$ ,  $d_{\bar{x}\bar{z}}$ ,  $d_{\bar{y}\bar{z}}$ ) where  $\bar{x}$ ,  $\bar{y}$ , and  $\bar{z}$  are the three octahedral axes. Ligand fields arising from hybridization lead to an energy separation between the doublet and triplet states of the order of 2 eV. The further reduction of the symmetry from  $O_h$  to  $D_{3d}$  does not additionally split the  $e_g$  states, which now form the  $e_g^\sigma$  doublet representation of  $D_{3d}$ . It does, however, split the  $t_{2g}$  triplet into an  $e_g^\pi$  doublet and an  $a_{1g}$  singlet with the  $e_g^\pi$ - $a_{1g}$  level splitting being typically smaller than the energetic separation to the  $e_g^\sigma$  doublet. Then to first order in the trigonal distortion, the basis functions for the  $e_g^\sigma$  representation are linear combinations of the familiar cubic-basis  $e_g$  states while the basis functions for the  $e_g^\pi$  and  $a_{1g}$  states are linear combinations of the familiar  $t_{2g}$  states (Table II) [50]. Lowering the symmetry below trigonal, in particular by breaking the  $C_3$  rotational symmetry about the axis perpendicular to the plane, will lift the degeneracies of the two  $e_g$  doublets. Such distortions may occur if the transition

TABLE II. Relationships among the atomic  $d$  orbitals for the standard cubic (tetragonal) basis with  $z$  aligned to the [001] direction shown in Fig. 1(b) and trigonal basis with  $z$  axis aligned to the [111] direction shown in Fig. 1(c). Note that in the absence of trigonal symmetry breaking, the  $a_{1g}$  and  $e_g^\sigma$  orbitals become degenerate and combine to transform as the  $t_{2g}$  representation.

Cubic basis [001]		Trigonal basis [111]		
Symmetry	Orbitals	Symmetry	Orbitals	
$t_{2g}$	$d_{\bar{x}\bar{y}}$	$a_{1g}$	$d_{z^2}$	
	$d_{\bar{y}\bar{z}}$		$e_g^\pi$	$\frac{2}{\sqrt{6}}d_{xy} + \frac{2}{\sqrt{3}}d_{yz}$
	$d_{\bar{x}\bar{z}}$		$e_g^\sigma$	$\frac{2}{\sqrt{6}}d_{x^2-y^2} - \frac{1}{\sqrt{3}}d_{xz}$
$e_g$	$d_{\bar{x}^2-\bar{y}^2}$	$e_g^\sigma$	$\frac{1}{\sqrt{3}}d_{x^2-y^2} + \frac{2}{\sqrt{6}}d_{xz}$	
	$d_{\bar{z}^2-\bar{r}^2}$		$\frac{1}{\sqrt{3}}d_{xy} - \frac{2}{\sqrt{6}}d_{yz}$	

metal valence is such that one of the orbital pairs forming a doublet is partially filled, enabling an electronic symmetry breaking transition.

### III. PHYSICS OF THE TRIGONAL DISTORTION IN $\text{TiCl}_2$

We now present density functional theory (DFT) calculations on the representative dihalide  $\text{TiCl}_2$  [51], using the experimental structure obtained from Inorganic Crystal Structure Database [46].  $\text{TiCl}_2$  exhibits a  $d^2$  electronic configuration and its primitive  $P\bar{3}m1$  structure contains a single formula unit. The Ti atoms are aligned along  $z$ , making for the simplest possible stacking. The Ti site symmetry is  $D_{3d}$ . Details of its crystal structure are presented in Table I.

We begin by analyzing nonmagnetic DFT calculations using the Perdew-Burke-Ernzerhof functional, in order to isolate the effect of the atomic structure on the on-site crystal field splittings and orbital order before performing further analysis. We then investigate correlation effects in the DFT+ $U$  approximation. This stepwise approach allows us to disentangle the effects of the structure from that of  $d$ -shell electron-electron interactions. We select different interlayer distances,  $X$ - $X$  distances, and  $L_2/L_1$  ratios to probe the trigonal symmetry effects on the orbital structure. We characterize the electronic structure changes via the on-site energy of the orbitals at the  $\Gamma$  point, and the orbital occupations, as obtained from the eigenvalues of the density matrix defined from orbital projectors.

Experimentally, these perturbations to the interlayer distance may be realized via external pressure, while the  $L_2/L_1$  ratio can be tuned via epitaxial strain. The effects we find pertain to  $\text{MX}_3$  compounds as well, as the  $\text{MX}_3$  structure can be obtained from the  $\text{MX}_2$  structure by removing 1/3 of the  $M$  atoms and keeping the ligand octahedral structure intact.

#### A. Level splittings and orbital occupancies

Figure 2 presents a summary of our results. Starting with the experimental structure, we find that the energy splitting at  $\Gamma$  corresponds to the expected 2-2-1 orbital splitting as shown by the vertical broken line in Figs. 2(a) and 2(b). Upon visualizing isosurfaces of the wave functions in real space at the  $\Gamma$  point (not shown), we find the orbitals represent wave functions of the trigonal basis. These wave functions are similar to the Wannier functions presented in Fig. 3. The lowest energy Ti  $d$ -derived state at  $\Gamma$  is the  $a_{1g}$  state. The wave function exhibits lobes directed through the faces parallel to the plane.

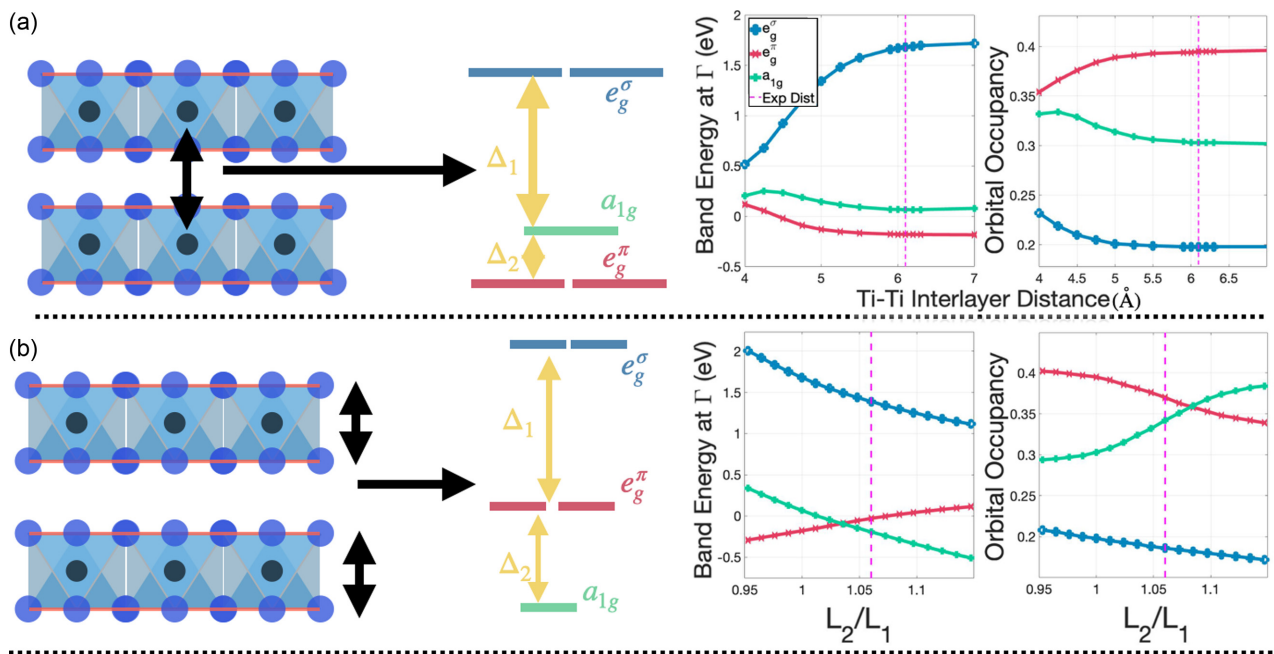


FIG. 2. Electronic orbital splitting at the nonmagnetic DFT level for  $\text{TiCl}_2$  as a function of (a) Ti-Ti interlayer distance and (b)  $L_2/L_1$  ratio, as quantified by crystal field splitting at the  $\Gamma$  point and orbital occupancy as obtained from the density matrix of the orbital projections. In (a), the octahedron is kept perfect ( $L_2 = L_1$ ), with a  $X$ - $X$  distance of 3.43 Å. In (b), the interlayer distance is kept fixed to the experimental value, while  $L_2/L_1$  is varied. The experimental interlayer distance and  $L_2/L_1$  ratio are indicated with broken magenta lines.

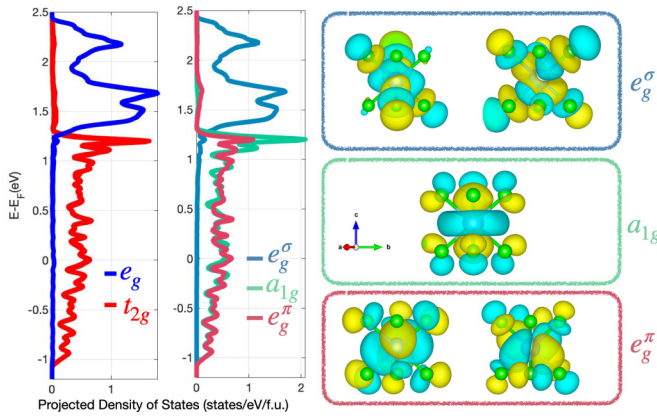


FIG. 3. Projected density of states for the Wannier functions for  $\text{TiCl}_2$  in the tetragonal basis (left) and trigonal basis (center), and eigenstates of the density matrix, as obtained by diagonalizing the density matrix (right). The crystal field splittings shown here are greatly increased in the presence of correlations and lead to a band gap opening in the presence of magnetism and correlations.

The next two higher energy states are the  $e_g^\pi$  doublet with wave-function lobes directed at the faces of the octahedron transverse to the plane. The highest energy states transform as the  $e_g^\sigma$  doublet in which the orbital lobes are directed along the octahedral axes, pointing towards the Cl anions. This behavior is expected because they behave equivalently to the  $e_g$  states of the cubic basis. The  $e_g^\sigma$ - $e_g^\pi$  splitting of approximately 1.5 eV is somewhat less than the approximately 2–3-eV splitting typical in perovskite transition metal oxides, reflecting the larger energy separation and weaker hybridization of the metal  $d$  states with the halogen ligand  $p$  states.

Next, we examine the effects on the electronic structure of varying the structural parameters (Fig. 2). We begin by fixing the  $\text{TiCl}_6$  octahedra to  $L_1 = L_2 = 3.430 \text{ \AA}$  with all  $M$ - $X$  bonds fixed to  $2.425 \text{ \AA}$  and vary the interlayer distance. We find that the crystal field splitting between the  $e_g^\sigma$  and the  $e_g^\pi/a_{1g}$  complex increases with increased interlayer distance as does the corresponding difference in orbital occupancy [Fig. 2(a)]. The  $e_g^\pi$ - $a_{1g}$  splitting is less dependent on the interlayer distance. For interlayer distances greater than or equal to the experimental value measured at ambient pressure, the crystal field splitting and orbital occupations converge to their asymptotic isolated layer values.

Next, we keep the interlayer distance fixed to the ambient pressure equilibrium experimental value of  $6.1 \text{ \AA}$  and vary the  $L_2/L_1$  ratio by displacing the Cl atoms along  $z$ . This changes  $L_2$  while keeping  $L_1$  the same. We find that increasing  $L_2$  increases the energy difference between the highest two and lowest three orbital states. In contrast to the effect of increasing the interlayer distance, changing  $L_2/L_1$  also decreases the  $a_{1g}$  orbital energy relative to the  $e_g^\pi$  energy. The occupancies change in the corresponding manner. The relative sizes of the energies and the orbital splittings, however, are not fixed. Importantly, we find that the critical  $L_2/L_1$  ratio at which the occupations are equal occurs at a different critical  $L_2/L_1$  ratio that gives a vanishing energy difference for  $e_g^\pi$ - $a_{1g}$  orbitals. Both correspond to  $L_2/L_1 \neq 0$ , underlining that the

symmetry of the representation of the Ti  $d$  shell is always at most trigonal, and never cubic.

### B. Orbital physics in the trigonal Wannier basis

Key to understanding the physical effects in a correlated material is an appropriate tight-binding model, which can be constructed via a Wannierization procedure as implemented in standard electronic structure codes. A Wannierization is in effect a choice of a basis that represents band states in a certain energy range, along with a projection of the density functional Hamiltonian onto this basis. It is desirable to choose a basis that is adapted to the physics of the problem at hand, both because an appropriate choice provides physical insight and because the form and magnitude of beyond-DFT interactions depend on the basis chosen.

Standard application of the WANNIER90 [52] code to di- and trihalide compounds tends to lead to the  $e_g$ - $t_{2g}$  basis functions well adapted to  $O_h$  symmetry, or other basis functions related through a linear transformation. To obtain Wannier functions adapted to the trigonal symmetry in a consistent way, we find it is best to first use WANNIER90 to obtain a basis, and then rotate the basis to obtain a diagonal density matrix. Another option is to diagonalize the Wannier Hamiltonian at the  $\Gamma$  point. A third choice is to diagonalize the on-site term in the real-space Wannier Hamiltonian. In most of the results presented here we employ the first basis choice (diagonalizing density matrix) which provides a more convenient representation. We note that this basis does not quite diagonalize the on-site term in the Wannier Hamiltonian, but the resulting small nonzero matrix elements cause no serious complication. To obtain real-space isosurfaces, we used the eigenvectors obtained by diagonalizing the density matrix to build a linear superposition of the Wannier functions obtained directly from WANNIER90. We have provided simple MATLAB scripts to do so in [47].

Figure 3 shows the density of states projected onto different combinations of the Wannier states obtained for  $\text{TiCl}_2$  in a standard application of WANNIER90 (left panel) and in the basis that diagonalizes the density matrix (center panel) after the rotation. The total density of states is the same in both cases. The  $e_g^\sigma$ -derived states, which are derived from the same functions in both cases, are approximately the same. The trigonal functions allow us to distinguish the higher-lying  $a_{1g}$  states from the lower-lying  $e_g^\pi$  states. Figure 3 also shows the corresponding isosurfaces of the resulting Wannier functions, which we obtain through linear mixing.

We now analyze the resulting Hamiltonian  $H_{\vec{R}_i}$  (Fig. 4), where the rows (columns) correspond to the following  $d$  orbitals: The first two correspond to  $e_g^\sigma$ , the middle one corresponds to  $a_{1g}$ , and the last two correspond to  $e_g^\pi$ . For  $\vec{R} = (0, 0, 0)$ , we find that the  $a_{1g}$  orbital is orthogonal to the other sets of orbitals in  $H_{\vec{R}_0}$ , similar to what is obtained in the atomic orbital projection matrix. While within the pairs of degenerate doublets the mixing is practically zero, there is however mixing between the two pairs. This  $H_{\vec{R}_0}$  however possesses the 2-2-1 pattern of eigenvalues consistent with  $D_{3d}$  symmetry.

As previously mentioned, one can also obtain a basis with the appropriate symmetry by diagonalizing this on-site

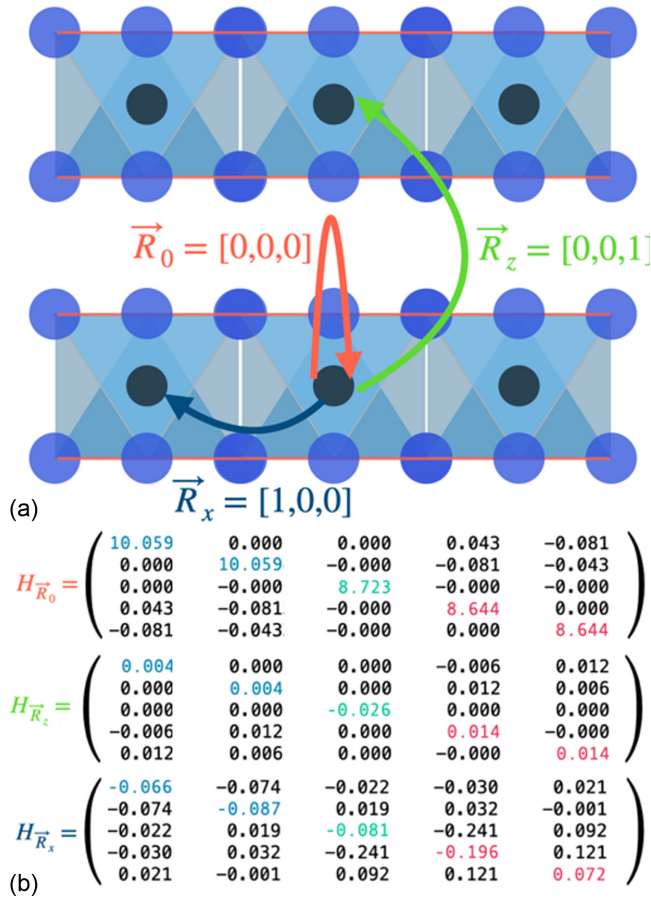


FIG. 4. (a)  $\vec{R}$  connecting transition metals  $M$ , for which we show the hopping matrices of the Hamiltonian below in (b). The diagonal elements are shown in blue for  $e_g^\sigma$ , in green for  $a_{1g}$ , and in red for  $e_g^\pi$ .

Hamiltonian; however, in that case, interorbital hoppings would lead to nonzero terms in the density matrix. Diagonalizing the density matrix instead provides a simpler description of orbitals and their filling without the additional complexity of off-diagonal terms, which becomes particularly useful in the presence of correlations where the atomic states can clearly be categorized as filled or empty (Sec. IV A). Second, the procedure of diagonalizing the density matrix is available and automatic for the density matrix obtained from the orbital projectors in most electronic structure codes.

Hopping along  $z$  between the Ti atoms  $\vec{R} = (0, 0, c)$  is primarily driven by  $a_{1g}$ - $a_{1g}$  hopping, hopping between the two pairs of doublet states, as well as small but nonzero hopping between equivalent orbitals as gleaned from  $H_{\vec{R}_z}$  in Fig. 4(b). Finally, hopping in plane between the atoms  $\vec{R} = (a, 0, 0)$  is driven by nonzero hoppings between all orbitals, however the lowest three orbitals in  $H_{\vec{R}_x}$  are the largest, as expected from the spatial orientation of the orbital lobes discussed previously. We also note that one of the eigenvalues of the hopping Hamiltonian is close to zero. The zero eigenvalue pertains to hopping among the highest two energy ( $e_g^\sigma$ ) orbitals. As a result, there will always be a weakly dispersing flat band among the higher  $e_g$  states along high symmetry directions in the zone.

$$H_{\vec{R}_0}^D = \begin{pmatrix} 10.065 & 0 & 0 & 0 & 0 \\ 0 & 10.065 & 0 & 0 & 0 \\ 0 & 0 & 8.724 & 0 & 0 \\ 0 & 0 & 0 & 8.639 & 0 \\ 0 & 0 & 0 & 0 & 8.639 \end{pmatrix}$$

$$H_{\vec{R}_0}^{\text{cubic}} = \begin{pmatrix} 10.046 & 0.052 & 0.053 & -0.148 & 0.023 \\ 0.052 & 8.656 & 0.022 & 0.022 & 0.052 \\ 0.053 & 0.022 & 8.691 & 0.015 & -0.104 \\ -0.148 & 0.022 & 0.015 & 8.711 & 0.192 \\ 0.023 & 0.052 & -0.104 & 0.192 & 10.029 \end{pmatrix}$$

FIG. 5. Wannier Hamiltonian at  $\vec{R} = (0, 0, 0)$  either after diagonalizing the on-site Hamiltonian or as obtained directly from WANNIER90 using an  $e_g$ - $t_{2g}$  model.

For comparison, we also provide the on-site Hamiltonians in two more bases (Fig. 5). First, we show  $H^D$ . Here, the on-site Hamiltonian has the same symmetry as the one obtained by diagonalizing the density matrix, and the eigenvalues are similar. Second, we provide the original Hamiltonian,  $H^{\text{cubic}}$ , obtained using a standard WANNIER90 procedure and used as a basis for the aforementioned trigonal procedure, which approximately exhibits  $e_g$ - $t_{2g}$  symmetry.

### C. Lower structural symmetries

Some of the dihalides and trihalides exhibit symmetries lower than trigonal. The point group  $C_{2h}$ , a subgroup of the trigonal point group  $D_{3d}$ , appears in both  $MX_2$  and  $MX_3$  compounds, namely, in  $ZrI_2$ , as well as in some polymorphs of  $RuCl_3$  and  $CrI_3$ . This symmetry reduction includes a breaking of the rotational symmetry, which splits the doublets, and may lead to minor mixing of the orbital eigenvalues; generally, subgroups of  $D_{3d}$  which do not maintain the three-fold rotational symmetry lead to a breaking of the doublets' degeneracy.

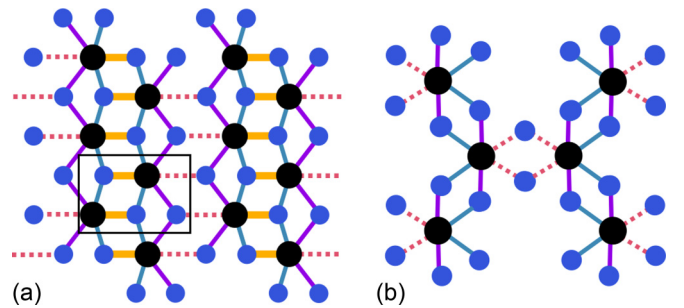


FIG. 6. Single layer lattice structure for materials with point group symmetry  $C_{2h}$ , which breaks the degeneracy of the doublets: (a) a layer of  $MX_2$ , with the structure from a layer of bulk  $ZrI_2$ , where the black rectangle represents the new unit cell, and (b) a layer of  $MX_3$ , with a similar pattern representing bulk layers, for example,  $RuCl_3$  and  $CrI_3$  with the  $AlCl_3$  structure type; all atoms in the sketch are within one unit cell. Distances between the atoms are indicated as follows: The red dotted lines are the longest, followed by purple, blue, then mustard yellow. The distortions characteristic of  $ZrI_2$  are much stronger than those of the  $MX_3$  materials. The  $M$  site symmetries are  $C_{1h}$  for panel (a) and  $C_2$  for panel (b). No  $d$  orbital degeneracies are enforced by either site symmetry, which leads to new possible states (e.g., those shown in Fig. 10).

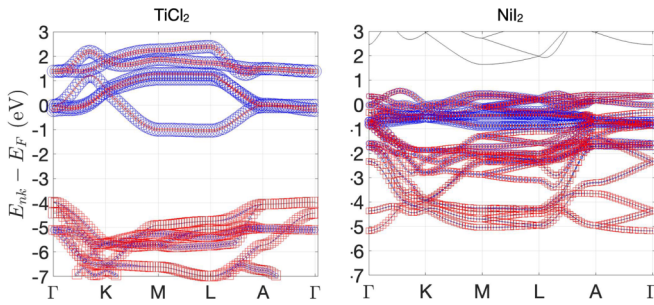


FIG. 7. DFT band structure and Wannier “fat bands” for a full  $p$ - $d$  model for (left)  $\text{TiCl}_2$  and (right)  $\text{NiI}_2$ , exemplifying materials that are in the Mott-Hubbard ( $\text{TiCl}_2$ ) and charge-transfer ( $\text{NiI}_2$ ) regimes. Blue circles correspond to transition metal  $M$   $d$  state projections; red squares correspond to ligand  $p$  states.

Figure 6 shows that the single layers of  $\text{ZrI}_2$  and  $\text{RuCl}_3$  or  $\text{CrI}_3$  no longer have threefold rotational symmetry. The in-plane lattice parameters defining the formula unit of a di- or trihalide lattice are no longer equivalent, and are replaced by perpendicular vectors describing the supercell that accommodates for this lower symmetry as described in the caption for the figure. This breaks the symmetry of the remaining two orbital doublet pairs. This symmetry reduction is associated with nonequivalence of both the  $X$ - $X$  bonds and the  $M$ - $X$  bonds as indicated in Fig. 6. In  $\text{ZrI}_2$  this is plainly discerned as the bond distortions are sufficiently strong that the structures can be understood to form 1D zigzag chains [53]. A minor mixing between the  $a_{1g}$  orbital and the other orbitals appears as a result of the symmetry lowering, and performing a Wannierization shows us that this minor mixing breaks its rotational symmetry.

The  $\text{ZrI}_2$  structure also has additional forms of symmetry breaking beyond that leading to the  $C_{2h}$  point group; for example, the two layers that form the minimum structural unit are not completely equivalent. The octahedral sizes differ between the layers. The symmetry of  $\text{ZrI}_2$  is even lower in certain experimentally reported structures with two nonequivalent octahedra forming each layer leading to point group  $C_{2v}$ . Such further symmetry reductions are beyond the scope of this paper.

#### IV. ELECTRONIC CORRELATIONS AND LOCAL STRUCTURE EFFECTS

Many transition metal compounds exhibit correlated insulating states. The correlation physics that produces these states tends to favor high spin, filled, and empty state configurations; the exact order is determined by a combination of correlation effects and electron-lattice coupling. Similar to perovskite oxides, 2D di- and trihalides can be in the Mott-Hubbard or in the charge-transfer regime of the Zaanen-Sawatzky-Allen (ZSA) classification [54].  $\text{TiCl}_2$  is a clear example of a Mott-Hubbard material as the  $d$  and  $p$  states are clearly separated by 4 eV [Fig. 7(a)]. Similar to the transition metal perovskite case, going right along the periodic table, i.e., towards higher orbital filling, the  $p$ - $d$  splitting decreases. In Fig. 7(b), we find the  $p$ - $d$  splitting is low for the well-known material  $\text{NiI}_2$  [55–57] with

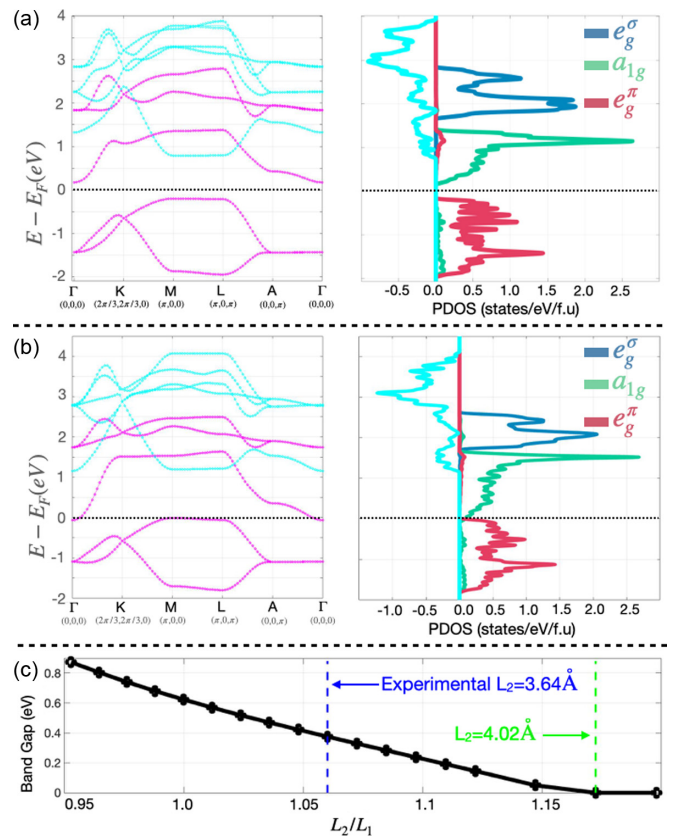


FIG. 8. Electronic band dispersions and orbital projected density of states for ferromagnetic, high-spin  $\text{TiCl}_2$  at the DFT+ $U = 2$  eV level: (a) experimental structure and (b) structure with  $L_2$  extended to 4.02 Å and interlayer distance kept constant. Left: Bands, majority spin in magenta, minority spin in cyan. Right: Projected density of states (PDOS), minority spin rescaled by dividing by 5. Increasing  $L_2/L_1$  closes the gap by reducing the orbital polarization of the lower three orbitals. (c) Dependence of the electronic band gap in  $\text{TiCl}_2$  with  $L_2/L_1$  ratio for a fixed interlayer distance.

the  $p$  and  $d$  bands overlapping in energy, corresponding to this insulating material being in the charge transfer regime.

#### A. Example of $\text{TiCl}_2$

We performed DFT+ $U = 2$  eV calculations on the dihalide  $\text{TiCl}_2$  in the experimental structure and allowed for spin symmetry breaking to gain initial insight into the role of correlations. To simplify the calculation and interpretation as much as possible, we use a single, three-atom unit cell, in the ferromagnetic state; other magnetic configurations may have different resulting states, but the general trends shown here would be consistent within a particular magnetic state. The Hubbard on-site Coulomb interaction allows the opening of a gap in the electronic spectrum ( $\approx 0.375$  eV), creating a fully orbital and spin polarized state [Fig. 8(a)]. While the effects of spin-orbit coupling may lower the amplitude of this band gap, we note that this effect is significant enough that it cannot be neglected in a realistic model of  $\text{TiCl}_2$ , or the halides more generally. Taking the  $\text{TiCl}_2$  experimental structure and allowing for spin symmetry breaking, we find a high spin, orbitally ordered state. The minority spin channel is completely

$$H_{R_0}^{U=2,\uparrow} = \begin{pmatrix} 9.906 & 0.000 & 0.000 & -0.001 & -0.002 \\ 0.000 & 9.906 & 0.000 & -0.002 & 0.001 \\ 0.000 & 0.000 & 8.716 & 0.000 & 0.000 \\ -0.000 & -0.002 & 0.000 & 6.979 & 0.000 \\ -0.002 & 0.001 & 0.000 & 0.000 & 6.979 \end{pmatrix}$$

FIG. 9. On-site  $\vec{R} = (0, 0, 0)$  Hamiltonian for the majority (spin up) channel for  $\text{TiCl}_2$  for  $U = 2$  eV and FM state, obtained from WANNIER90 followed by a rotation that diagonalizes the  $d$  orbital density matrix, similar to Fig. 4. Note that the Hamiltonian is nearly diagonal, and the crystal field splittings are strongly amplified by correlations.

unoccupied. Electronic correlations and magnetism strongly enhance the crystal field splittings, as observed in the on-site Hamiltonian in Fig. 9, where the splitting between the  $e_g^\sigma$  and the  $a_{1g}$  orbitals is now comparable to that between the  $a_{1g}$  and the  $e_g^\pi$  and over 1 eV. Two electrons reside in the majority spin channel of the two  $e_g^\pi$  orbitals, while the  $e_g^\sigma$  and  $a_{1g}$  occupations are essentially zero.

Calculations with structures obtained by elongating  $L_2$  while keeping  $L_1$  constant result in a closing of the gap, while shortening  $L_2$  further opens the gap, by shifting the relative energy levels of the lowest three states (Fig. 8). Similar effects can be obtained by changing the interlayer distance as well. Importantly, we note that in the presence of electronic correlations the electronic configuration favors the state that leads to fully occupied and empty states and the opening of a band gap, and a strong trigonal distortion is needed to counteract this effect. We note that, in a tetragonal basis, as discussed before, the lower three  $t_{2g}$  states would remain equivalent, as their lobes would point along equivalent directions, which would obscure the identity of the active orbitals—the singlet and doublet—participating in the band gap opening.

The trigonal basis corresponding to a diagonal orbital density matrix has the advantage of simplifying the physical

description with electronic states that are either filled or empty and have no off-diagonal terms. It also provides a consistent way to build a basis as we vary the structural parameters, which can be numerically difficult to obtain directly from WANNIER90 without the additional rotation performed here. We further note that we were not able to obtain a cubic  $e_g-t_{2g}$  basis in this case, likely due to the large crystal field splitting between the  $a_{1g}$  state and the lower  $e_g^\pi$  states.

## B. Survey of broken symmetry phases

By varying the transition metal ion and considering both dihalides and trihalides, one can obtain all  $d^n$  configurations ranging from  $d^1$  ( $\text{TiI}_3$ ) to  $d^9$  ( $\text{CuCl}_2$ , proposed below). As a result, a range of correlated insulating states can be produced, as shown in Fig. 10. Some of these states will involve orbital order that breaks the trigonal symmetry, leading to the appearance of one-dimensional lattice structures—or, more generally, structures that break the threefold rotational symmetry.

In the  $d^1$  configuration the natural Mott insulating state involves an electron in the  $a_{1g}$  orbital. This state preserves the trigonal symmetry. However, the multiple superexchange pathways that also involve  $e_g^\pi$  orbitals suggest that unless  $L_2/L_1$  can be made very small the ground state will be ferromagnetic. However, if the  $L_2/L_1$  ratio can be made large enough, a change in level ordering may occur and it is possible to have an orbitally ordered Mott insulator with one electron in the  $e_g^\pi$  orbitals and a corresponding orbital order and trigonal symmetry breaking lattice distortion.

In the  $d^2$  case, we may generically expect a high spin ground state with two electrons in the  $e_g^\pi$  orbitals, as found in the DFT+ $U$  calculations for  $\text{TiCl}_2$ . For a small enough  $L_2/L_1$  ratio, however, a state with one electron in the  $a_{1g}$  orbital and one in the  $e_g^\pi$  doublet may lift the trigonal symmetry.

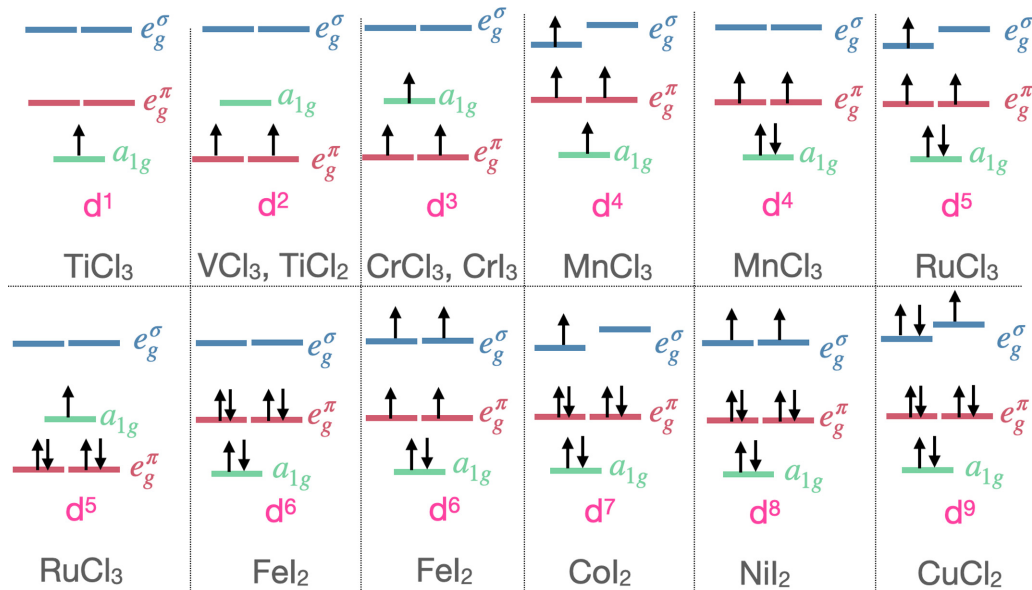


FIG. 10. Different possible electronic states for  $d^1-d^9$  occupations as discussed in the main text. Configurations that break the doublet degeneracy would be associated with further lattice distortions, reducing symmetry below trigonal, including structural modes as described in Fig. 6. States with higher  $a_{1g}/e_g^\pi$  occupation ratios are likely to have a higher  $L_2/L_1$  ligand bond ratio.



The relatively smaller ligand field splitting in the halides relative to the octahedral perovskite oxides suggests that the  $d^4$ ,  $d^5$ , and  $d^6$  states will all be high spin. The  $d^4$  and  $d^6$  configurations would also exhibit orbitally ordered and trigonally broken states;  $d^6$  can also support an insulating diamagnetic state with the gap opened by the crystal field splitting between the two higher energy and lower three orbitals.

The  $d^7$  state is most likely to be a  $S = 1/2$  state with the lowest three orbitals fully occupied, and one of the  $e_g^\sigma$  orbitals half filled and spin polarized, likely leading to a structurally broken state of the form found in the materials with  $C_{2h}$  point symmetry. The  $d^8$  configuration is most likely to be a  $S = 1$  state with each  $e_g^\sigma$  orbital half filled and spin polarized. In some scenarios, it may be orbitally polarized and nonmagnetic, associated with a symmetry breaking mode in the lattice, most likely as previously discussed.

Such configurations may be susceptible to MITs, which we assess using a recently devised machine-learning classification model [58]—particularly as machine learning is becoming increasingly important in correlated materials' understanding and discovery [59]. We found that the binary MIT–non MIT classifier tends to predict that most of the 2D halides are candidate MIT compounds, giving a positive MIT classification for  $\text{CrCl}_3$ ,  $\text{FeCl}_3$ ,  $\text{IrBr}_3$ ,  $\text{MnCl}_2$ ,  $\text{RuCl}_3$ ,  $\text{TiCl}_2$ ,  $\text{VCl}_3$ , and  $\text{ZrI}_2$ , and a negative classification for  $\text{CrI}_3$ ,  $\text{FeI}_2$ , and  $\text{NiI}_2$ . This is likely due to the similarity of this class of materials to perovskite oxide MIT transition compounds in the structural features exhibited, such as the average transition metal–ligand distances which range between 2.4 and 3.01 Å, the metal–metal distances of 3.3–4.2 Å, and electronic descriptors, e.g., estimated unscreened Hubbard  $U$  values. However, due to their intrinsic broken symmetry and reduced dimensionality, these materials generally will be exclusively insulating. Additionally, the screened interaction parameters are likely to be higher than in the three-dimensional (3D) perovskites, due to lower screening in this class of materials [60]—and van der Waals materials more generally. Similar to MIT compounds, the 2D halides will tend to display coupled electronic and lattice transitions at low temperatures [31].

For the  $d^9$  and possibly  $d^4$  configurations, the presence of one hole in the  $e_g^\sigma$  manifold implies a breaking of rotational symmetry and, likely, a one dimensional electronic structure. To examine this possibility, we perform the following simulation. We take a single layer of the experimental  $\text{ZrI}_2$  structure and replace Zr with Cu and I with Cl without allowing the structure to relax. Owing to the strong charge-transfer character of the resulting theoretical material, the Cu  $d$  manifold is mostly filled. Nonetheless, after performing the appropriate rotation of the  $d$ -shell basis, we find that the two least-occupied orbitals are  $e_g^\sigma$ -like (Fig. 11). These orbitals display nonzero orbital polarization with one orbital with  $d_{x^2-y^2}$  character pointing along Cu–Cl bonds along the 1D chain, and one orbital of  $d_{3z^2-r^2}$  character pointing towards Cu–Cl bonds that connect the 1D chains. This type of symmetry breaking can likely be exploited, provided the appropriate material strains, to form 1D conducting chains out of a 2D structure. This behavior is similar to how the pseudo-2D electronic structure of cupratelike high-temperature superconductors forms from out of 3D conducting building blocks. Another orbitally polarized

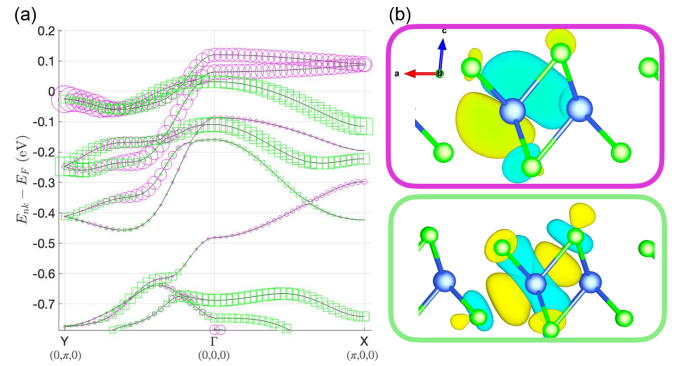


FIG. 11. (a) DFT band structure, and fat bands of the top two Wannier orbitals on the hypothetical  $\text{CuCl}_2$  monolayer discussed in the main text. (b) Real-space isosurfaces of the highest energy  $d$  orbitals, with occupations 0.912 and 0.93 per spin channel. Due to the pseudo-1D nature of the symmetry broken lattice structure, there is relatively little dispersion along the  $\Gamma$ - $X$  direction.

state can also be obtained with a different orbital basis for the  $d^9$  configuration [61].

## V. CONCLUSIONS AND DISCUSSION

We showed that the highest possible metal orbital symmetry of 2D dihalides and trihalides comprising edge-shared  $\text{MX}_6$  octahedra is trigonal, and analyzed the interplay of atomic lattice, orbital physics, and correlation effects. Within this trigonal basis, we showed that the amplitude of the electronic orbital splittings can be tuned both by the interlayer distance as well as through changing the ligand–ligand bond ratio  $L_2/L_1$ , and that the effect of correlations strongly favors ordered, insulating states, by further enhancing the crystal field splittings resulting from the trigonal symmetry. We have shown that this effect is very large, of the order of 0.1–1.0 eV, and cannot be neglected in any realistic modeling of this class of materials.

In addition, the orbital occupancies can be sensitively tuned through changes in these atomic structure features, which can be achieved experimentally via pressure, via strain, as well as possibly via optical excitations of the relevant structural modes to enable control of magnetic configurations and other electronic ordering, justifying why these materials are most likely to be insulating. We showed that these materials can be analyzed from the point of view of the ZSA classification.

We showed how one can build and analyze a Wannier model corresponding to this reduced symmetry, symmetry which can lead to novel (correlated) electronic states. Our paper building these Wannier functions is however general, and can be applied to other materials with different symmetries as well, and we have provided simple scripts to do so. Our paper serves as a basis to understand correlated phenomena in this class of materials, and their interplay with lattice symmetry modes, and easily allows for models to disentangle their roles—similar to recently built models on perovskites and their Ruddlesden–Popper phases [11,17,62,63]. Our results may be particularly important in the search for candidate spin liquids. Spin liquid states are predicted to be found in the vicinity of a Mott transition and in symmetric highly

frustrated structures. Our generic finding of strong orbital ordering and associated trigonal symmetry breaking will be important in appropriately modeling—and discovering—potential spin liquids and other novel states.

#### ACKNOWLEDGMENTS

This research was supported in part by the National Science Foundation under DMREF Grant No. DMR-1729303. The information, data, and work presented herein were funded

in part by the Advanced Research Projects Agency-Energy, U.S. Department of Energy, under Grant No. DE-AR0001209. A.J.M. is supported in part by Programmable Quantum Materials, an Energy Frontier Research Center funded by the U.S. Department of Energy, Office of Science, Basic Energy Sciences, under Grant No. DE-SC0019443. The views and opinions of authors expressed herein do not necessarily state or reflect those of the U.S. Government or any agency thereof. The Flatiron Institute is a division of the Simons Foundation.

- 
- [1] D. G. Schlom, L. Q. Chen, C. B. Eom, K. M. Rabe, S. K. Streiffer, and J. M. Triscone, *Annu. Rev. Mater. Res.* **37**, 589 (2007).
- [2] V. Garcia, M. Bibes, L. Bocher, S. Valencia, F. Kronast, A. Crassous, X. Moya, S. Enouz-Vedrenne, A. Gloter, D. Imhoff, C. Deranlot, N. Mathur, S. Fusil, K. Bouzehouane, and A. Barthelemy, *Science* **327**, 1106 (2010).
- [3] Y. Qi and K. M. Rabe, [arXiv:2103.16466v2](https://arxiv.org/abs/2103.16466v2).
- [4] H. Chen, Q. Qiao, M. S. J. Marshall, A. B. Georgescu, A. Gulec, P. J. Phillips, R. F. Klie, F. J. Walker, and C. H. Ahn, *Nano Lett.* **14**, 4965 (2014).
- [5] Y. Tokura, *Curr. Opin. Solid State Mater. Sci.* **3**, 175 (1998).
- [6] M. Gibertini, M. Koperski, A. F. Morpurgo, and K. S. Novoselov, *Nat. Nanotechnol.* **14**, 408 (2019).
- [7] S. Koohfar, A. B. Georgescu, A. N. Penn, J. M. LeBeau, E. Arenholz, and D. P. Kumah, *npj Quantum Mater.* **4**, 25 (2019).
- [8] H. J. A. Molegraaf, J. Hoffman, C. A. F. Vaz, S. Gariglio, D. Van Der Morel, C. H. Ahn, and J. M. Triscone, *Adv. Mater.* **21**, 3470 (2009).
- [9] Y. Mizuguchi, F. Tomioka, S. Tsuda, T. Yamaguchi, and Y. Takano, *Appl. Phys. Lett.* **93**, 152505 (2008).
- [10] S. Koohfar, A. B. Georgescu, I. Hallsteinsen, R. Sachan, M. A. Roldan, E. Arenholz, and D. P. Kumah, *Phys. Rev. B* **101**, 064420 (2020).
- [11] A. B. Georgescu and A. J. Millis, *Commun. Phys.* **5**, 135 (2022).
- [12] G. G. Guzmán-Verri, R. T. Brierley, and P. B. Littlewood, *Nature (London)* **576**, 429 (2019).
- [13] J. Shamblin, M. Heres, H. Zhou, J. Sangoro, M. Lang, J. Neufeind, J. A. Alonso, and S. Johnston, *Nat. Commun.* **9**, 86 (2018).
- [14] P. Zubko, S. Gariglio, M. Gabay, P. Ghosez, and J.-M. Triscone, *Annu. Rev. Condens. Matter Phys.* **2**, 141 (2011).
- [15] M. Först, A. D. Caviglia, R. Scherwitzl, R. Mankowsky, P. Zubko, V. Khanna, H. Bromberger, S. B. Wilkins, Y. D. Chuang, W. S. Lee, W. F. Schlotter, J. J. Turner, G. L. Dakovski, M. P. Miniti, J. Robinson, S. R. Clark, D. Jaksch, J. M. Triscone, J. P. Hill, S. S. Dhesi *et al.*, *Nat. Mater.* **14**, 883 (2015).
- [16] M. Medarde, P. Lacorre, K. Conder, F. Fauth, and A. Furrer, *Phys. Rev. Lett.* **80**, 2397 (1998).
- [17] A. B. Georgescu, O. E. Peil, A. S. Disa, A. Georges, and A. J. Millis, *Proc. Natl. Acad. Sci. USA* **116**, 14434 (2019).
- [18] C. Domínguez, A. B. Georgescu, B. Mundet, Y. Zhang, J. Fowlie, A. Mercy, A. Waelchli, S. Catalano, D. T. Alexander, P. Ghosez, A. Georges, A. J. Millis, M. Gibert, and J. M. Triscone, *Nat. Mater.* **19**, 1182 (2020).
- [19] D. Lee, B. Chung, Y. Shi, N. Campbell, F. Xue, K. Song, J. P. Podkaminer, T. H. Kim, P. J. Ryan, T. R. Paudel, J. W. Spinuzzi, D. A. Tenne, E. Y. Tsymlal, M. S. Rzechowski, L. Q. Chen, J. Lee, and C. B. Eom, *Science* **362**, 1037 (2018).
- [20] A. D. Caviglia, M. Först, R. Scherwitzl, V. Khanna, H. Bromberger, R. Mankowsky, R. Singla, Y. D. Chuang, W. S. Lee, O. Krupin, W. F. Schlotter, J. J. Turner, G. L. Dakovski, M. P. Miniti, J. Robinson, V. Scagnoli, S. B. Wilkins, S. A. Cavill, M. Gibert, S. Gariglio *et al.*, *Phys. Rev. B* **88**, 220401(R) (2013).
- [21] N. J. Szymanski, L. N. Walters, D. Puggioni, and J. M. Rondinelli, *Phys. Rev. Lett.* **123**, 236402 (2019).
- [22] J. H. Chu, H. Kue, J. Analytis, and I. Fisher, *Science* **337**, 710 (2012).
- [23] P. A. Lee, N. Nagaosa, and X. G. Wen, *Rev. Mod. Phys.* **78**, 17 (2006).
- [24] M. R. Norman, *Physics* **13**, 85 (2020).
- [25] S. Gariglio, N. Reyren, A. D. Caviglia, and J. M. Triscone, *J. Phys.: Condens. Matter* **21**, 164213 (2009).
- [26] B. Keimer, S. A. Kivelson, M. R. Norman, S. Uchida, and J. Zaanen, *Nature (London)* **518**, 179 (2015).
- [27] J. N. Nelson, N. J. Schreiber, A. B. Georgescu, B. H. Goodge, B. D. Faeth, C. T. Parzyck, C. Zeledon, L. F. Kourkoutis, A. J. Millis, A. Georges, D. G. Schlom, and K. M. Shen, *Sci. Adv.* **8**, eabj0481 (2022).
- [28] C. Huang, F. Wu, S. Yu, P. Jena, and E. Kan, *Phys. Chem. Chem. Phys.* **22**, 512 (2020).
- [29] S. Son, M. J. Coak, N. Lee, J. Kim, T. Y. Kim, H. Hamidov, H. Cho, C. Liu, D. M. Jarvis, P. A. C. Brown, J. H. Kim, C. H. Park, D. I. Khomskii, S. S. Saxena, and J. G. Park, *Phys. Rev. B* **99**, 041402(R) (2019).
- [30] S. Tian, J. F. Zhang, C. Li, T. Ying, S. Li, X. Zhang, K. Liu, and H. Lei, *J. Am. Chem. Soc.* **141**, 5326 (2019).
- [31] E. Gati, Y. Inagaki, T. Kong, R. J. Cava, Y. Furukawa, P. C. Canfield, and S. L. Bud'ko, *Phys. Rev. B* **100**, 094408 (2019).
- [32] B. Lyu, Y. Gao, Y. Zhang, L. Wang, X. Wu, Y. Chen, J. Zhang, G. Li, Q. Huang, N. Zhang, Y. Chen, J. Mei, H. Yan, Y. Zhao, L. Huang, and M. Huang, *Nano Lett.* **20**, 6024 (2020).
- [33] M. An, Y. Zhang, J. Chen, H. M. Zhang, Y. Guo, and S. Dong, *J. Phys. Chem. C* **123**, 30545 (2019).
- [34] R. Yadav, N. A. Bogdanov, V. M. Katukuri, S. Nishimoto, J. Van Den Brink, and L. Hozoi, *Sci. Rep.* **6**, 37925 (2016).
- [35] T. Yokoi, S. Ma, Y. Kasahara, S. Kasahara, T. Shibauchi, N. Kurita, H. Tanaka, J. Nasu, Y. Motome, C. Hickey, S. Trebst, and Y. Matsuda, *Science* **373**, 568 (2021).
- [36] H. Suzuki, H. Liu, J. Bertinshaw, K. Ueda, H. Kim, S. Laha, D. Weber, Z. Yang, L. Wang, H. Takahashi, K. Fürsich, M. Minola,

- B. V. Lotsch, B. J. Kim, H. Yavaş, M. Daghofer, J. Chaloupka, G. Khaliullin, H. Gretarsson, and B. Keimer, *Nat. Commun.* **12**, 4512 (2021).
- [37] H. Li, T. T. Zhang, A. Said, G. Fabbris, D. G. Mazzone, J. Q. Yan, D. Mandrus, G. B. Halász, S. Okamoto, S. Murakami, M. P. M. Dean, H. N. Lee, and H. Miao, *Nature (London)* **12**, 3513 (2021).
- [38] H. Takagi, T. Takayama, G. Jackeli, G. Khaliullin, and S. E. Nagler, *Nat. Rev. Phys.* **1**, 264 (2019).
- [39] M. Hermanns, I. Kimchi, and J. Knolle, *Annu. Rev. Condens. Matter Phys.* **9**, 17 (2018).
- [40] M. A. McGuire, *Crystals* **7**, 121 (2017).
- [41] D. Wang and B. Sanyal, *J. Phys. Chem. C* **125**, 18467 (2021).
- [42] T. Kong, S. Guo, D. Ni, and R. J. Cava, *Phys. Rev. Materials* **3**, 084419 (2019).
- [43] X. Chen, X. Fan, L. Li, N. Zhang, Z. Niu, T. Guo, S. Xu, H. Xu, D. Wang, H. Zhang, A. S. McLeod, Z. Luo, Q. Lu, A. J. Millis, D. N. Basov, M. Liu, and C. Zeng, *Nat. Phys.* **16**, 631 (2020).
- [44] G. F. Dionne, in *Magnetic Oxides* (Springer, New York, 2009), pp. 37–106.
- [45] A. S. Botana and M. R. Norman, *Phys. Rev. Materials* **3**, 044001 (2019).
- [46] M. Hellenbrandt, *Crystallography Reviews* **10**, 17 (2004).
- [47] <https://github.com/alexandrub53/Wannier90HamiltonianTools>.
- [48] S. V. Streltsov and D. I. Khomskii, *Phys. Usp.* **60**, 1121 (2017).
- [49] N. Wagner, R. Seshadri, and J. M. Rondinelli, *Phys. Rev. B* **100**, 064101 (2019).
- [50] Note that for the cubic case the conventional coordinate system involves a  $z$  axis chosen parallel to an  $M$ - $X$  bond while for the trigonal case the conventional coordinate system involves a  $z$  axis passing through an octahedral face (i.e., along  $[111]$  in conventional octahedral coordinates).
- [51] DFT calculations were performed using the QUANTUM ESPRESSO software package on a three atom formula unit, using ultrasoft pseudopotentials using the PBE exchange-correlation functional, an energy cutoff of 748 eV, and a  $20 \times 20 \times 20$   $k$  grid. Orbital occupations were obtained using the orthonormal atomic projections, as implemented in QUANTUM ESPRESSO; DFT+ $U$  calculations were performed with the  $U$  applied to orthonormal atomic projections as well using the simplified Dudarev + $U$  formalism.
- [52] A. A. Mostofi, J. R. Yates, G. Pizzi, Y. S. Lee, I. Souza, D. Vanderbilt, and N. Marzari, *Comput. Phys. Commun.* **185**, 2309 (2014).
- [53] D. H. Guthrie and J. D. Corbett, *J. Solid State Chem.* **37**, 256 (1981).
- [54] J. Zaanen, G. A. Sawatzky, and J. W. Allen, *Phys. Rev. Lett.* **55**, 418 (1985).
- [55] C. R. Ronda, G. J. Arends, and C. Haas, *Phys. Rev. B* **35**, 4038 (1987).
- [56] H. Starnberg, M. Johnson, and H. Hughes, *J. Phys. C* **19**, 2689 (1986).
- [57] G. van der Laan, J. Zaanen, G. A. Sawatzky, R. Karnatak, and J. M. Esteve, *Phys. Rev. B* **33**, 4253 (1986).
- [58] A. B. Georgescu, P. Ren, A. R. Toland, S. Zhang, K. D. Miller, D. W. Apley, E. A. Olivetti, N. Wagner, and J. M. Rondinelli, *Chem. Mater.* **33**, 5591 (2021).
- [59] J. Fowlie, A. B. Georgescu, B. Mundet, J. del Valle, and P. Tückmantel, *Front. Phys.* **9**, 725853 (2021).
- [60] Y. Yekta, H. Hadipour, E. Sasioglu, C. Friedrich, S. A. Jafari, S. Blugel, and I. Mertig, *Phys. Rev. Materials* **5**, 034001 (2021).
- [61] H. Qin, J. Chen, B. Sun, Y. Tang, Y. Ni, Z. Chen, H. Wang, and Y. Chen, *Phys. Chem. Chem. Phys.* **23**, 22078 (2021).
- [62] O. E. Peil, A. Hampel, C. Ederer, and A. Georges, *Phys. Rev. B* **99**, 245127 (2019).
- [63] Q. Han and A. Millis, *Phys. Rev. Lett.* **121**, 067601 (2018).